Microstructures and wear-corrosion performance of vacuum plasma sprayed and cold gas dynamic sprayed Muntz alloy coatings

C.J. Huang, K. Yang, N. Li, W.Y. Li, M.P. Planche, C. Verdy, H.L. Liao, G. Montavon

Microstructures and wear-corrosion performance of vacuum plasma sprayed and cold gas dynamic sprayed Muntz alloy coatings

C.J. Huang [a,b*], K. Yang [c], N. Li [c], W.Y. Li [c*], M.P. Planche [a], C. Verdy [a], H.L. Liao [a], G. Montavon [a]

[a] ICB UMR 6303, CNRS, Univ. Bourgogne Franche-Comté, UTBM, F-90100 Belfort, France.

[b] iMMC-IMAP, Université catholique de Louvain, 1348 Louvain-la-Neuve, Belgium.

[c] State Key Laboratory of Solidification Processing, Northwestern Polytechnical University, 710072 Xi'an, P.R. China.

* Corresponding authors: chunjie.huang@uclouvain.be (C.J. Huang)

Abstract:

As one of the important Cu alloys, brass has been implanted in many fields of architecture or fabrication industry. Muntz (Cu60Zn40) brass alloy was used to manufacture the brass coatings in this study due to showing the best corrosion resistance. Two different spray methods i.e. vacuum plasma spray (VPS) and cold gas dynamic spray (CGDS), were chosen to perform the synthesis of brass coatings aiming to avoid oxidation. Upon utilization of VPS and CGDS techniques, spray process is crucial to the microstructures, phase transformation, mechanical property, and wear and corrosion properties of Muntz alloy coatings. Here results show that no oxidation was characterized in both two processes. Nevertheless, a vaporization of 19.32 wt. % Zn occurred during VPS, which would lead to the significant differences in grain size, misorientation distribution, texture and phase composition of VPSed coating from those of CGDSed coating. The CGDSed coating exhibited excellent performances due to a preservation of chemical composition of original feedstock. For example, it yielded a hardness value of 211.8 ± 9.8 $HV_{0.3}$, which was nearly two times higher than that of VPSed coating (119.3 ± 11.6 $HV_{0.3}$). It was also shown that a significant wear rate reduction ((1.3 ± 0.018)×10^{-5} *v.s.* (2.36 ± 0.39)×10^{-4} mm^3/mN) and a corrosion resistance enhancement.

Keywords: Vacuum plasma spray; Cold gas dynamic spray; Muntz alloy; Microstructure; Wear; Corrosion.

Abbreviations and symbols

Abbreviation

PS	Plasma spray	EDS	energy-dispersive X-ray spectroscopy
APS	Atmospheric plasma spray	SEM	Scanning electron microscope
VPS	Vacuum plasma spray	OM	Optical microscope
AS	Arc spray	EBSD	Electron backscatter diffraction
CGDS	Cold gas dynamic spray	XRD	X-ray diffraction
HVOF	High-velocity oxygen fuel	TBs	Twinned boundaries
EIS	Electrochemical impedance spectroscopy	OCP	Open circuit potential
GB	Grain boundary	HAGBs	High-angle grain boundaries
LAGBs	Low-angle grain boundaries	CSL	Coincidence site lattice

Symbol

r	Radius of worn track, mm	E_{corr}	Corrosion potentials, V
S	Cross-sectional area, mm	i_{corr}	Corrosion current density, $\mu A\ cm^{-2}$
p	Load, N	l	Sliding distance, m
β_a	Anodic Tafel slope, $V\ dec^{-1}$	β_c	Cathodic Tafel slope, $V\ dec^{-1}$

1 Introduction

Thermal spray, a group of coating processes in which metallic and non-metallic materials deposited in a molten or semi-molten condition to form a coating, is divided into several processes according to the thermal energy source and the kinetic energy of the sprayed materials, such as electric arc spray (AS), plasma spray (PS), and high velocity oxy-fuel (HVOF) spray. Among these processes, PS is mainly divided into atmospheric plasma spray (APS) and vacuum plasma spray (VPS) according to an operating pressure range [1]. During APS, a coating is formed in an open-air environment. Therefore, the metallic coating is easily oxidized and its density will be decreased due to a number of pores [1,2]. With respect to VPS, it can prevent a coating from the oxidation and improves the coating density, since molten droplets will undergo a low atmospheric pressure and a high velocity. Consequently, this kind of Cu coating prepared *via* VPS generally exhibits the better mechanical properties compared to other thermal spraying processes [3,4] as shown in Fig. 1, due to a typical lamellar and dense microstructure, a low porosity and a limited oxygen content.

Acting as a new member of the thermal spray technique, cold gas dynamic spray (CGDS), based on supersonic fluid dynamics and high-speed impact dynamics, is a relatively new solid-state coating process [5-10]. During CGDS, the sprayed powder particles (commonly in a size range of 5-50 μm) are accelerated to a higher velocity changing from 300 to 1200 m/s in a high-speed gas jet, and projected onto a substrate or a previously deposited layer in a nominally solid state (i.e. at a temperature well below the melting point of the

powder). CGDS features a higher particle velocity and a lower processing temperature, showing many advantages compared to these conventional thermal spray techniques [9]. For example, the heating effects on both substrates and sprayed powders are rarely observed, since the coating deposition will not allow an explosion of the substrates or sprayed materials to a very high temperature, which will make it possible to deposit this kind of the temperature-sensitive materials without any significant changes in the microstructure of feedstock [5]. In addition, the resulting residual stresses are typically low and mostly compressive compared to thermal spraying, which permits a deposition of relatively thick coatings.

The Cu-based alloys, as one of the most versatile engineering materials with numerous excellent properties, such as high strength, good heat conductivity, good corrosion and biofouling resistance, good machinability and ductility [5], have been widely applied within the industrial and electronic fields [6]. Therefore, based on this aim of well developing these coatings, many comparative investigations on preparing Cu and its alloys coatings between conventional thermal spray and cold gas dynamic spray have been disclosed. For example, in Gärtner and Stoltenhoff's studies [3,7], the sprayed Cu particles were completely molten during the arc spray or at least partially molten during the high-velocity oxygen fuel (HVOF) spray. While the CGDSed Cu coating showed a denser microstructure without melting and oxidation, which might suggest that a deposition of Cu using CGDS showed a prominent advantage over these conventional thermal spray processes. Similarly, Li et al. [10] also used VPS and CGDS to obtain the dense Cu-4Cr-2Nb coatings, and almost no oxidation occurred for both depositions. Furthermore, Gassot et al. [4] compared the process of VPS with APS and HVOF and studied the influences of these processes on the microstructures and properties of Cu coatings, indicating that VPSed coating showed a recrystallized structure with the least oxygen content and this was very different from the typical splat structures of APS and HVOF coatings [3,4].

As one of the best-known Cu alloys, bronze has been used as the anti-corrosion and anti-friction coating materials, such as bearings and lubricant materials. A fabrication of bronze alloy coatings and their composite coatings have been obtained by electro deposition [11], thermal spray [12,13] and cold gas dynamic spray [13-15]. For instance, the microstructures and wear performances of bronze-based coatings deposited by APS and CGDS have been investigated by Miguel et al. [13], and showing that the CGDSed bronze coatings exhibited

a higher sliding wear resistance due to a better cohesion, a higher matrix hardness and better distribution of fine alumina.

On the other hand, the brass alloys showing excellent properties (lightness, mechanical strength, corrosion resistance, etc), have extended to numerous applications, such as architectures, industrial fabrication, maritime, etc. [16]. However, the brass coatings were mainly prepared by electro-deposition [17,18]. The studies on preparing the brass coatings was given a very small number of attempts to manufacture them with thermal spray processes [19], which will seriously limit its numerous applications in many fields. Muntz brass alloy with a two-phase (α+β) structure, patented in 1832 by George F. Muntz [20], has showed many interesting properties [21]. Owing to maintaining an anti-corrosion property with a lower cost, Muntz alloy has recently became the main material for boat sheathing and propeller, which work under a marine environment. Thus, the thermal sprayed methods featuring of high deposition rate and rapid manufacturing are essential to facilitate the application of brass coatings. Thus, herein, we selected the Muntz alloy powder for preparing the non-oxidized and dense brass coatings using the vacuum plasma deposition process, compared with the solid-state process of cold spray [22]. The effects of spray processes (VPS and CGDS) on the microstructures, the phases and the wear and corrosion resistances of the Muntz alloy coatings were compared and explored.

2. Experimental procedure

2.1 Powder

Fig. 2 shows the surface and cross-sectional morphologies of the gas-atomized Muntz alloy powder (ECKA Granules Metal Powders Ltd., UK). An irregular shape is obviously shown in Fig. 2. The SEM cross-sectional morphology of a single non-etched Cu60Zn40 particle appears free of porosity (Fig. 2c). An average grain size of 2.1 μm was estimated upon etching (Fig. 2d). The chemical composition of Cu60Zn40 alloy powder was detailed in Table 1.

A size distribution of used Muntz powder was measured with a Mastersizer 2000 laser particle size distribution, showing a Gaussian size distribution ranging from +15.1 to -69.7 μm with an average diameter of 35.6 μm (Fig. 3). The powder was used to be directly deposited without an optimization of powder morphology.

2.2 Coating deposition

VPS was carried out using a Metco A-2000 VPS equipment (Sulzer Metco F4-VB plasma torch, Switzerland) under a low-pressure condition. The working gases were argon and hydrogen with an arc current of 720 A and an electrical plasma power of 43 kW. The substrate surface temperature was measured to be about 800 ^{o}C by a monochromatic pyrometer (Land Infrared type M2). The standoff distance from the nozzle exit to the substrate surface was 250 mm. The coating was deposited on E355 steel plates, which were sand-blasted with the SiO_2 powder under ambient condition. Optimized processing parameters of VPS are summarized in Table 2.

CGDS was carried out using a commercial Kinetic 3000 system (CGT GmbH, Germany). This installation consists of a control cabinet, a gas heater, a powder feeder and a spray gun equipped with different nozzles (Laval nozzle) depending on the nature of the material to be sprayed. The nozzle (MOC-24, CGT) having a cylindrical section was used in this study. The brass coatings were deposited on the Cu alloy plates, which were sand-blasted with the SiO_2 powder under the ambient condition. To achieve the optimal processing parameters and best quality of Muntz coatings, various parameters were tested for CGDS process. Gas temperature were changed from 250 ^{o}C to 550 ^{o}C and gas pressure was fixed at 2.8 MPa. The selecting principle is based on maximum density and low manufacturing cost. The relative density of CGDS Muntz coating was measured by an analytical balance based on Archimedes principle. Detailed optimized parameters of CGDS process used in this work are provided in Table 3.

2.3 Characterizations

The morphologies of powder and the microstructural and phase characterizations of the coatings were measured by an optical microscope (OM, Nikon, Japan) and scanning electron microscope (SEM, JSM5800LV, JEOL, Japan) equipped with an electron backscatter diffraction (EBSD) system. The phase composition of sprayed coatings was characterized by X-ray diffraction (XRD). The chemical composition of the powder and the coatings was quantified using the SEM equipped with energy-dispersive X-ray spectroscopy (EDS, Oxford Instruments INCA system, UK). The coating microhardness was tested by a Vickers hardness (Leitz, Germany) indenter with a load of 3 N for 15 s, and more than 20 values were randomly tested and averaged to evaluate the coating hardness.

Friction tests were performed on a ball-on-disk CSM tribometer under an ambient condition (temperature: 19 °C, humidity: 53 %). Before friction tests, all deposit surfaces were polished to a roughness (Ra) of about 0.2 μm. The counterpart was a 6 mm diameter 100Cr6 steel ball with a mirror finished surface. The friction force was measured with a sensor and dynamically recorded into a computer. The friction coefficient was computed when the friction force was divided by the applied load. The applied load and sliding velocity were 5 N and 0.1 m/s, respectively. The diameter of the worn track and the sliding distance were 6 mm and 30 m, respectively. The wear rate defined as the worn volume per unit of normal load and sliding distance was calculated using the equation below:

$$v_r = \frac{2\pi r S}{p \times l}$$

where r (mm) is the radius of worn track. S (mm^2) is the cross-sectional area of the track circle. p (N) is the load, and l (m) is the sliding distance. After the completion of 30 m sliding distance, the cross-sectional area of the worn track was measured using an Altisurf 500 profilometer with the given average values corresponding to a set of 5 random positions along the worn track for each sample.

All electrochemical measurements were carried out using a standard three-electrode that are exposed to an electrolyte of a non-deaerated and unstirred 3.5 wt. % NaCl aqueous solution at ambient temperature. Prior to the electrochemical testing, all coatings removed from the substrates were ground with abrasive papers up to 2000 grit, and finally rinsed in an ultrasonic bath with acetone. The coating was used as the working electrode immersed in the solution, and a platinum foil and a saturated calomel electrode served as the counter electrode and reference electrode, respectively. The open circuit potential (OCP) was first recorded in a three-electrode cell and a steady state OCP was reached after immersing in the test solution for 1.5 hours. And then Tafel polarization curves were plotted by starting scanning electrode potential from -0.25 V to +0.25 V versus OCP at a scanning rate of 0.167 mV/s. Electrochemical impedance spectroscopy (EIS) was performed with a voltage amplitude of ± 5 mV in the frequency ranging from 0.01 to 100 kHz. Corrosion current densities (i_{corr}) were estimated from the Tafel extrapolation of the cathodic and anodic slopes using Power Suite software. EIS measurements were repeated three times in order to insure fare discussions and the ZView software was used for the fitting of the resulted spectra..

3. Results and discussion

3.1 Element composition

Elemental mapping of the original powder analyzed by EDS (red colour representing Cu, green color representing Zn) shows a considerable amount of 59.45 wt.% Cu (Fig. 4a), which is consitent with the comercially technical data (58.5-61.5 wt. %). After ungergoing a high-temperature and low-pressure deposition process of VPS, the composition proportion of Cu element increased because of a significant loss of 19.32 wt. % Zn under the present experiment condition. Generally, Zn element has the relatively lower melting point (419.5 ^{o}C) and boiling point (907 ^{o}C). Therefore, a vaporization of Zn is very easily occurred. This phenomenon is similar to the physical vacuum dealloying process, which is commenly used to fabricate the three-dimensional porous metals [23]. However, a dense structure was formed in the VPSed coating as shown in Fig. 4b. When observed the Fig. 4c, the Cu element composition shows a similar result to that of the original powder, which is attributed to the fact that the deposition of CGDS takes place through the intensive plastic deformation of particles upon impact in a solid state at a temperature well below the melting point of spray material. Consequently, the deleterious effects of oxidation, decomposition, and melting inherent in the thermal spraying could be eliminated [24].

3.2 Coating microstructures

The typical cross-sectional microstructures of Muntz alloy coatings via VPS and CGDS are shown in Fig. 5. A homogeneous appearance and a dense microstructure (porosity: 0.35 %) are observed in the VPSed coating (Fig. 5a). This microstructure is composed of molten and semi-molten particles, which is similar to the lamellar structure [4]. Additionally, a recrystallized structure has been produced due to the high temperature during VPS, which suggests that the metallurgical bonding is main bonding mechanism as shown in Fig. 5b. As indicated by Gassot et al. [4], a recrystallized structure was presented in the VPSed coating with very low oxygen content, which was different from those of the deposited coatings by APS and HVOF. As for the VPSed coating, the molten and semi-molten particles have experienced a coupled effect of zinc vaporization and rapid solidification under the high impact velocity. The remaining Zn was dissolved in the Cu, and forming a substitutional solid solution of Zn in Cu. As also known, a formation of the substitutional solid solutions between Cu and Zn is governed by the Hume-Rothery rules. The solubility of a metal with higher

valence in a solvent lower valence is more compared to the reverse situation (i.e. Zn is much more soluble in Cu). Furthermore, the low stacking fault energy of Cu-Zn alloys contributes to forming the fine twins in the solid solution, as distinguished inside the particles presented by the inset in Fig. 5b.

As for the CGDSed coating, the Muntz particles are deformed and elongated, and the distorted particles are bonded to the adjacent ones (Fig. 5c). A presence of interface between these interlocked particles is noticeable, which is taken into account the mechanical bonding mechanism in the CGDSed coating [7]. However, when compared to the microstructure of the pure copper coatings [7,10], the deformability of Cu-Zn particles is not sufficient to fill in all the gaps between the deposited particles owing to the relatively higher hardness, which leads to a presence of pores and non-bonded interfaces in CGDSed coating (porosity: 1.12 %). When observed in the etched state (Fig. 5d), the impact-induced deformation twins are clearly shown in the interior particle as marked by the arrow.

EBSD investigations were performed for studying the detailed microstructures of the VPSed and CGDSed coatings. EBSD reconstructed orientation maps and grain size distribution of these two coatings are shown in Fig. 6. The VPSed coating shows a recrystallized structure of fine grains with an average grain size of 0.35 μm (Fig. 6a), which is due to the presence of high temperature in VPSed coating inducing a uniform interdiffusion and recrystallization. Therefore, the oxide layers are not observed, thus forming a uniform coating. By contrast, the CGDSed coating exhibits a flattened structure with an average grain size of 1.9 μm (Fig. 6b). Some Cu60Zn40 particles are extremely elongated and distorted into the long strips while others remains undistorted, suggesting an heterogeneous plastic deformation during the deposition process. Furthermore, it is clearly that the high-velocity impact effect results in a fact that grains near the interface are smaller than those in the interior due to the dynamic recrystallization [24,25]. Thus, the grains near the particle boundaries are oriented, which are surround by the interior of deposited particle. Moreover, certain defects (e.g., relatively large pores) are also observed due to an insufficient deformation in the sprayed coating process, which will result in a poor bonding structure.

We applied the detailed pole figures for twinned microstructure characterizations (see white circle in Fig. 6a). In the <110> pole figure, clusters of purple and pink spots correspond to the fine grains in EBSD map are clearly seen. Three <110> directions (both purple and pink) located on the coherent (111) twin plane (a red

arc) are shared by the twinned and untwined regions. This twinned nature can also be evidenced in <111> pole figure, where the direction circled is a common <111> direction to both purple and pink grain. The (111) twin plane corresponding to this common <111> direction, is also indicated by a red arc in this pole figure. Clearly, those three pairs of non-common directions have a symmetric relation with respect to the twin plane.

The grain boundary (GB) map of the VPSed coating and the misorientation angles distribution are shown in Figs. 7a and 7b, respectively. As can be seen, a recrystallization is resulted from the high temperature of the plasma jet and the rapid solidification during VPS, which is responsible for the generation of these fine grains. Considering all GBs misorientation angles that are bigger than are 2°, the VPSed coating shows a large number of high-angle grain boundaries (HAGBs) at a fraction of 84.36 % and a small quantity of low-angle grain boundaries (LAGBs) at a fraction of 15.64 %. The LAGBs are accumulated in the certain regions, while other regions show a more uniform and larger grain distribution in the VPSed coating. This phnomenen could be ascribled to a high substrate temperature produced by the long plasma jet, causing a self-annealing of the deposited particles. Indeed, this self-annealing is beneficial, because it provides stress relief and recrystallization, resulting in an enhanced interparticle bonding [26]. Therefore, these regions with less LAGBs accumulation and larger grain formation could be induced by the self-annealing effect. On the other hand, a fraction of 71 % of HAGBs (red lines in Fig. 7a) are responsible for the Coincidence Site Lattice (CSL) Σ3 boundaries due to the recrystallization in the VSP process, because massive annealing twins occurred around 60 ° after VPS (Fig. 7b).

The GB map of the CGDSed coating is shown in Fig. 7c, and the corresponding distribution of misorientation angles is shown in Fig. 7d. The CSed coating is characterized by HAGBs at a fraction of 22.6 %, and LAGBs remaining at a fraction of 78.4 %, because a high density of dislocations and sub-grains are presented in the extensively deformed particles after impact. When a particle with a sufficient high-velocity impact upon the substrate or on previously deposited particles [21], a large number of dislocations accumulate near the grain boundaries, which might be responsible for the HAGBs in these intensively elongated grains [27,28].

3.3 Microtextures

The microstructure evolutions induced by the plastic deformation during the impact is closely related to the changes in the texture. Thus, the texture distribution in the coatings fabricated by VPS and CGDS need to be well investigated. A comparison of the orientation data obtained for the VPSed and CGDSed coatings is presented in Fig. 8, in the form of <100>, <110> and <111> pole figures. It is found that VPSed coating shows a homogeneous texture, suggesting that the preferred orientation is reduced or even eliminated due to the coupled effects of recovery of stress relief and recrystallization during VPS [26]. However, the CGDSed coating shows a little stronger crystallographich texture after an intensively plastic deformation.

3.4 Phase transformation

The structural and compositional analysis of the Muntz powder, and the VPSed and CGDSed coatings were carried out by the XRD patterns as shown in Fig. 9. Original powder is consisted of β' phase due to the rapid solidification in the gas atomization. However, only α diffraction peak is detected after VPS, and this is due to the vaporization of Zn element and the formation of α solid solution. Compared to the CGDSed coating, it is consisted of two main phases, i.e. α and β', which is very different from that of the powder and the VPSed coating, thus implying that CGDS induces structural changes and phase transformations. Because a severe plastic deformation at high strain rate combined with high pressures are up to more than 10 GPa, and are extremely high cooling rates [28]. Furthermore, the peak widths of the CGDSed coating are also broadened, which is perhaps caused by the formation of sub-grains and micro-strain (see Fig. 7c). As for the VPSed coating, the increased peak intensity indicates a higher crystallite size. Furthermore, the increased twins in the α grains (see Fig. 7a) will lead to a right shift of α-phased peaks.

For a further identification in the phase evolution, the EBSD phase maps were used to characterize the phase transformation. The twin distribution and the phase map are shown in Figs. 10a and 10c. The twins are represented by the yellow lines, and the red, bule and yellow regions are respective to the α, γ and β' phases. The annealing twins are uniformly presented with only α phase after VSP as shown in Fig. 10a. Furthermore, a little non-equilibrium phase of γ-Cu_5Zn_8 (blue color) with a complex cubic structure is presented in these regions of a higher concentration of Zn due to the thermo-mechanical effect. However, compared to the CGDSed coating, two solid solutions in the coating, i.e. the majority of α and a little β' intermetallic phase, are

shown in the Fig. 10c. In the α-phase, the presence of twins in the CGDSed coating is marked by the black arrow, which is attributed to the highly impact induced deformation.

3.5 Microhardness

A typical Vicker indentation for the VPSed and CGDSed coatings under the force of 3 N are characterized by the regular shape as illustrated in the Fig. 11. In addition, the VPSed coating shows a noticeable increment in the indentation size compared to that of the CGDSed coating, which implies that the VPSed coating has a lower resistance to the compressive load. In Li's previous study, it was indicated that some cracks were formed during the indentation process, which might be due to the weak particle interfaces [29]. However, it is not the same case in the present work, which suggests a good resistance in both coatings.

A comparison of the microhardness value for the VPSed and CGDSed coatings with a corresponding EDS analysis for the indentations are shown in Fig. 12. The microhardness measurements on the CGDSed coating yields the value of 211.8 ± 9.8 $HV_{0.3}$, which is nearly two times higher than that of the VPSed coating (119.3 ± 11.6 $HV_{0.3}$). In addition, the hardness value of the CGDSed coating is much higher than the bronze coating of CuSn8, and comparable to that of the TiN/CuSn8 composite coating fabricated by cold spray [30]. The significantly higher hardness in CGDSed coating is due to the strain-hardening effect during the particle impact [31]. On the other hand, the solid solutions depending on the proportion of Zn element may also have an effect on the microhardness [32]. In addition, the lower hardness of the VPSed coating is ascribed to the stress relief and the disapperance of β' intermetallic phase during the self-annealing and Zn vaporization process.

3.6 Wear behavior

3.6.1 Friction coefficient and wear rate

The COF evolution for the VPSed and CGDSed coatings with the sliding time during the dry sliding wear contact test is shown in Fig. 13a. After a very short run-in period, both COFs arrives at a relatively steady state. The COF of the VPSed coating shows a much higher value than that of the CGDSed coating. For VPSed coating, the COF is approximately between 0.57 and 0.9. While in the case of the CGDSed coating, it shows a quite stable and low value of 0.19. The higher COF of the VPSed coating is produced due to the lower

281 microhardness compared to that of the CGDSed coating [33]. Fig. 13b illustrates the wear rates of the two
282 coatings. As can be seen that the CGDSed coating shows a reduced wear rate ((1.3 ± 0.02)×10^{-5} mm^3/mN) by
283 more than one order of magnitude compared to that of the VPSed coating ((2.36 ± 0.39)×10^{-4} mm^3/mN). This
284 suggests a higher wear resistance of the CGDSed coating, and it is also correlated well with the higher
285 microhardness of the CGDSed coating [34]. The significant discrepancies in the increasing the COF and the
286 decreasing the wear rate of CGDS coating are related to the tribological mechanism.

287 **3.6.2 Wear mechanism**

288 Fig. 14a shows an overview of worn track of the VPSed coating. The distribution of the Cu, Zn, O and Fe
289 elements across this worn track is obtained from the result of EDS line profilng (Fig. 14b). The scan position
290 is indicated using a yellow line in Fig. 14a. The EDS line profilng indicates that no occurrence of oxdication
291 was occurred during the friction test. Cu and Zn elements are homogeneously distributed within the track. In
292 addition, some brim-liked shapes are observed on the worn surface of VPSed coating, which are closely
293 related to the stick-slip motion feature of the sliding ball. When repeated under the shear forces, the cracks
294 would be produced at this interface in the direction perpendicular to the sliding direction and finally, material
295 can be detached from the coating. In such a case, the adhesion, between the deposit and the sliding ball, is a
296 dominant factor for the tribological behavior. Those brim-liked shapes are assumed to be formed by the
297 superior deformation of the deposit surface parallel to the sliding direction. Indeed, this phenomenen occurs
298 under the combined conditions of large adhesion force between the sliding pair and low hardness but high
299 ductibility of the VPSed coating.

300 However, the worn surfaces and the elements distribution of the CGDSed coating indicate a different
301 tribological mechanism. There is no obvious evidence of delamination on the worn surface of the CGDSed
302 coating. The wear behavior of the CGDSed coating is featured of micro-abrasive and micro-plowing proved
303 by the worn surface. The CGDSed coating shows a strain-hardened microstructure with the hard and brittle
304 phase of β', resulting in decreasing the plasticity and reducing the adhesive wear. Hence, the worn surface of
305 the CGDSed coating presents a relatively smooth morphology after the friction test.

3.7 Electrochemical behavior

Tafel polarization and EIS diagrams were utilized to explore the corrosion behaviors of the VPSed anc CGDSed coatings in 3.5 wt. % NaCl solution. Fig. 15 shows the Tafel polarization curves of the VPSed and CGDSed coatings. The Tafel curve parameters, e.g. corrosion potentials (E_{corr}), corrosion current density (i_{corr}), anodic Tafel slope (β_a) and cathodic Tafel slope (β_c) were extracted using Tafel's extrapolation; the results are present in Table 4.

The spray process has a significant influence on the polarization characteristic of the obtained coatings. The VPSed coating shows a higher E_{corr} value (-0.218 V) than that of CGDSed coating (-0.345 V) due to an excessive loss of Zn (the standard electrode potentials: E_{Zn}= - 0.763 V and E_{Cu}= + 0.337 V). Generally, more positive E_{corr} reflects the higher degree of thermodynamically corrosion resistance of materials [35]. In addition, the cathodic Tafel slopes (β_c) of both coatings are higher than anodic Tafel slopes (β_a), suggesting that they are dominated by the cathode reaction [36]. Furthermore, the current density used to assess the kinetics of corrosion reactions, is essentially proportional to the corrosion rate. The i_{corr} values of the VPSed coating (i_{corr}= 0.783 µA/cm^2) coating is higher than that of the CGDSed coating (i_{corr}= 0.235 µA/cm^2), indicating that a lower corrosion rate and a higher corrosion resistance in CGDSed coating than that of the VPSed coating. In fact, electrochemical process of galvanic coupling plays a more significant effect on the dezincification corrosion in the VPSed coating, because the lower fraction of Zn (20.54 %). In addition, the phenomenon of passivation occurs due to the film formation on the VPSed coating surface.

To further investigate the corrosion performances of the two brass coatings by different spray methods, AC impedance spectroscopy was also monitored. EIS analysis are presented as both Nyquist (Fig. 16a) and Bode (Fig. 16b) plots of the VPSed and CGDSed coatings obtained experimentally at their corresponding OCPs. As for the VPSed coating, the Nyquist plot consists of a single semicircle correlating to the charge transfer process at higher frequencies and a Warburg line correlating to the diffusion of reactants toward or away from the surface at lower frequencies. This suggests the corrosion mechanism of the VPSed coating is controlled by both the charge transfer and the diffusion process. In addition, the diameters of semicircles of the CGDSed coating is larger than that of the VPSed coating, which implies that the CGDSed coating shows the higher charge transfer resistance and thus the better corrosion resistance. Thus CGDSed coating has much higher

impedance value than that of the VPSed coating as indicated by the Bode plot in the Fig. 16b. The Nyquist and Bode plots are quite well in agreement with the polarization behaviors.

4 Conclusions

In this study, a vacuum deposition process as VPS and a solid-state deposition process as CGDS, were chosen for depositing Muntz alloy coatings to avoid oxidation. Microstructures and key properties of coatings are comparatively studied, and main conclusions are that: A significant vaporization of 19.32 wt. % Zn occurred during VPS, while CGDSed coating showed a similar element composition to that of the original powder. The VPSed coating (porosity: 0.35 %) shows a dense and a recrystallized microstructure with an average grain size of 0.35 μm. While the CGDSed coating (porosity: 1.12 %) exhibits a flattened structure (average grain size of 1.9 μm) with the presence of pores and non-bonded interfaces The VPSed coating has a large number of HAGBs at 84.36 % (71 % of HAGBs are CSL Σ3 boundaries) and a few LAGBs at 15.64 %. The CGDSed coating is characterized by HAGBs at 22.6% and LAGBs in the remaining 78.4 %, showing a high density of dislocations and sub-grains in the deformed grains. The VPSed coating exihibites a homogeneous texture, indicating that the preferred orientation is reduced or even eliminated due to the self-annealing effect during VPS. However, the CGDSed coating shows similar crystallographich texture after an intensively plastic deformation. Only α diffraction peak was detected after VPS due to the vaporization of zinc and formation of α solid solution. However, the CGDSed coating is consisted of α and β' because of the severe plastic deformation at high strain rate.The microhardness of the CGDSed coating yields the value of 211.8 ± 9.8 $HV_{0.3}$, which was two times higher than that of the VPSed coating (119.3 ± 11.6 $HV_{0.3}$). While in the case of CGDSed coating ((1.3 ± 0.02)×10^{-5} mm^3/mN), it shows a reduced wear rate by more than one order of magnitude compared to that of the VPSed coating ((2.36 ± 0.39)×10^{-4} mm^3/mN). The galvanic corrosion significantly affects the dezincification corrosion in the VPSed coating owing to its higher fraction of copper, which is in agreement with the higher impedance of CGDSed coating.

Acknowledgements

The C.J. Huang author would like thank the support from the program of CSC (201404490058). The W.Y. Li author would like thank the support from the program of the National Natural Science Foundation of China (51574196) and the 111 Project (B08040).

References

[1]. Y.R. Niu, D. Lu, L.P. Huang, J. Zhao, X.B. Zheng, G. Chen. Vacuum. 117 (2015) 98-103.

[2]. C.Z. Zhai, Y.R. Niu, L.P. Huang, H.H. Pan, H. Li, X.B. Zheng, J.L. Sun. Ceramics Inter. 42 (2016) 18798-18805.

[3]. T. Stoltenhoff, C. Borchers, F. Gärtner, H. Kreye. Surf. Coat. Tech. 200 (2006) 4947-4960.

[4]. H. Gassot, T. Junquera, V. Ji, M. Jeandin, V. Guipont, C. Coddet, C. Verdy, L. Grandsire. Surf. Eng. 17 (2001) 317-322.

[5]. J.C. Liu, X.L. Zhou, X. Zheng, H. Cui, J.S. Zhang. Appl. Surf. Sci. 258 (2012) 7490-7496.

[6]. Y.F. Sun, N. Xu, H. Fujii. Mater. Sci. Eng. A. 589 (2014) 228-234.

[7]. F. Gärtner, T. Stoltenhoff, J. Voyer, H. Kreye, S. Riekehr, M. Koçak. Surf. Coat. Tech. 200 (2006) 6770-6782.

[8]. S. Yin, Y.C. Xie, J. Cizek, E. Ekoi, T. Hussain, D. Dowling, R. Lupoi. Compos. Part Eng. B. 113 (2017) 44-54.

[9]. C.Y. Chen, S. Gojon, Y.C. Xie, S. Yin, C. Verdy, Z.M. Ren, H.L. Liao, S.H. Deng. Surf. Coat. Tech. 309 (2017), 719-728.

[10]. W.Y. Li, X.P. Guo, C. Verdy, L. Dembinski, H.L. Liao, C. Coddet. Scripta Mater. 55 (2006) 327-330.

[11]. T. Nickchi, M. Ghorbani, A. Alfantazi, Z. Farhat. Mater. Des. 32 (2011) 3548-3553.

[12]. K. Venkatesarlu, V. Rajinikanth, T. Naveen, D.P. Sinha, Atiquzzaman, A.K. Ray. Wear. 266 (2009) 995-1002.

[13]. J.M. Miguel, J.M. Guilemany, S. Dosta. Surf. Coat. Tech. 205 (2010) 2184-2190.

[14]. H. Na, G. Bae, S. Shin, S. Kumar, H. Kim, C.H. Lee. Composit. Sci. Tech. 69 (2009) 463-468.

[15]. X.P. Guo, G. Zhang, W.Y. Li, Y. Gao, H.L. Liao, C. Coddet. Appl. Surf. Sci. 255 (2009) 3822-3828.

[16]. H. Imai, S.F. Li, K. Kondoh, Y. Kosaka, T. Okada, K. Yamamoto, M. Takahashi, J. Umeda. Mater. Trans. 55 (2014) 528-533.

[17]. V. Vignal, V. Rault, H. Krawiec, A. Lukaszczyk, F. Dufour. Electrochimica Acta, 203 (2016) 416-425.

[18]. V. Rault, V. Vignal, H. Krawiec, O. Tadjoa. Corros. Sci. 86 (2014) 275-284.

[19]. M.R. Dastan, G.H. Khalaf. J. Eng. 08 (2018) 53-58.

[20]. H.S. Rawdon, Typical cases of the deterioration of Muntz metal (60-40 brass) by selective corrosion, Washington, D.C.: Dept. of Commerce, Bureau of Standards: 1918.

[21]. A. Tuthill, Guidelines for the use of copper alloys in sea water, NiDl Pubilication, 1988.

[22]. C.J. Huang, W.Y. Li, Y. Feng, Y.C. Xie, M.P. Planche, H.L. Liao, G. Montavon. Mater. Character. 125 (2017) 76-82.

[23]. Y.X. Sun, Y.B. Ren, K. Yang. Mater. Lett. 165 (2016) 1-4.

[24]. W.Y. Li, C.J. Li, G.J. Yang. Appl. Surf. Sci. 257 (2010) 1516-1523.

[25]. Y. Zou, W. Qin, E. Irissou, J.G. Legoux, S. Yue, J.A. Szpunar, Scripta Mater. 61 (2009) 899-902.

[26]. S. Sampath, H. Herman. J. Therm. Spray. Tech. 5 (1996) 445-456.

[27]. C. Borchers, F. Gartner, T. Stoltenhoff, H. Kreye. Acta Mater. 53 (2005) 2991-3000.

[28]. H. Assadi, H. Kreye, F. Gartner, T. Klassen. Acta Mater. 116 (2016) 382-407.

[29]. W.Y. Li, H.L. Liao, J.L. Li, C. Coddet. Adv. Eng. Mater.10 (2008) 746-749.

[30]. X.P. Guo, G. Zhang, W.Y. Li, Y. Gao, H.L. Liao, C. Coddet. Appl. Surf. Sci. 255 (2009) 3822-3828.

[31]. C.J. Huang, W.Y. Li. Surf. Eng. 32 (2016) 663-669.

[32]. A. Moshkovich, V. Perfilyev, I. Lapsker, L. Rapoport. Wear, 3210 (2014) 34-40.

[33]. A. Rahbar-kelishami, A. Abdollah-zadeh, M.M. Hadavi, A. Banerji, A. Alpas, A.P. Gerlich. Mater. Des. 86 (2015) 98-104.

[34]. X.P. Guo, G. Zhang, W.Y. Li, L. Dembinski, Y. Gao, H.L. Liao, C. Coddet. Appl. Surf. Sci. 254 (2007) 1482-1488.

[35]. J.Z. Kong, T.J. Hou, Q.Z. Wang, L. Yin, F., Zhou, Z.F. Zhou, L.K.Y. Li. Surf. Coat. Tech. 307 (2016) 118-124.

[36]. G. Venkatasubramanian, S. Mideen, A.K. Jha. Res. J. Chem. Sci. 3 (2013) 74-80.

Tables

Table 1. Chemical composition of Muntz brass alloy powder (wt. %).

Elements	Cu	Fe	Pb	Sn	Zn
Composition	58.5 - 61.5	≤ 0.15	0.25 - 0.7	≤ 0.26	bal.

Table 2. Optimized parameters of VPS used in this work.

Pressure	Arc current	Arc voltage	Argon gas flow rate	Hydrogen flow rate	Powder gas flow rate	Powder feed rate	Spray distance
100 Pa	720 A	60 V	50 NL/min	5 NL/min	3 NL/min	15 g/min	250 mm

Table 3. Optimized parameters of CGDS used in this work.

Pressure	Temperature	Standoff distance	Hatch distance	Nozzle moving speed	Propulsive gas
2.8 MPa	450 °C	30 mm	5 mm	20 mm/s	Compressed air

Table 4. Electrochemical parameters obtained from Tafel polarization curves of VPSed and CGDSed coatings.

Process	E_{corr}(V_{SCE})/V	i_{corr}/(μA·cm^{-2})	β_c/(V·dec^{-1})	β_a/(V·dec^{-1})
VPS	- 0.218	0.783	0.065	0.039
CS	- 0.345	0.235	0.141	0.052

Figures

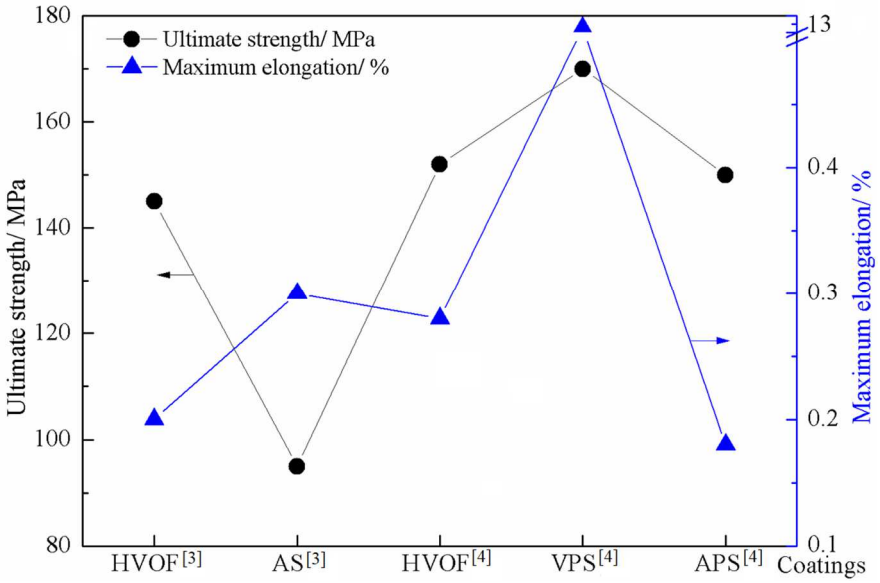

Fig. 1. Mechanical resistance and elongation of Cu coatings by thermal spraying [3,4].

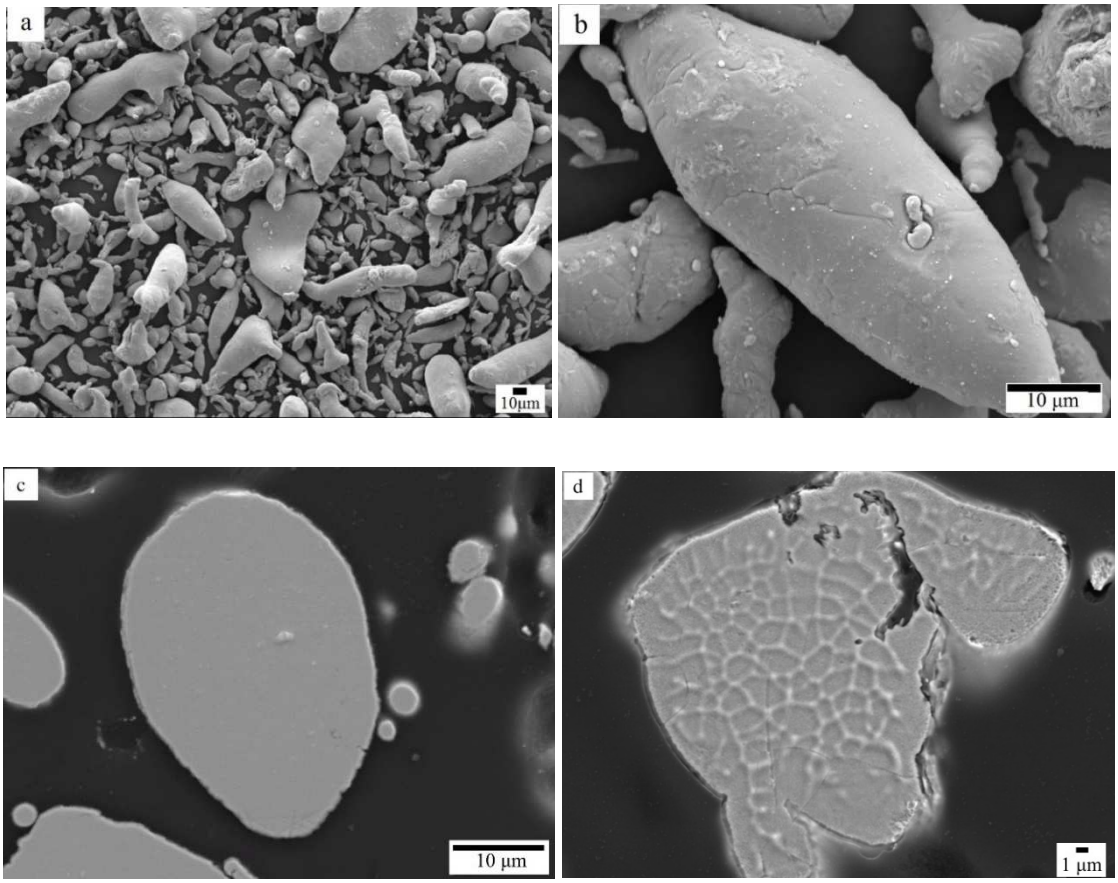

Fig. 2. SEM micrographs of (a) the used Muntz alloy powder and (b) high magnification of a particle, (c) non-etched and (d) etched cross-section of a single particle.

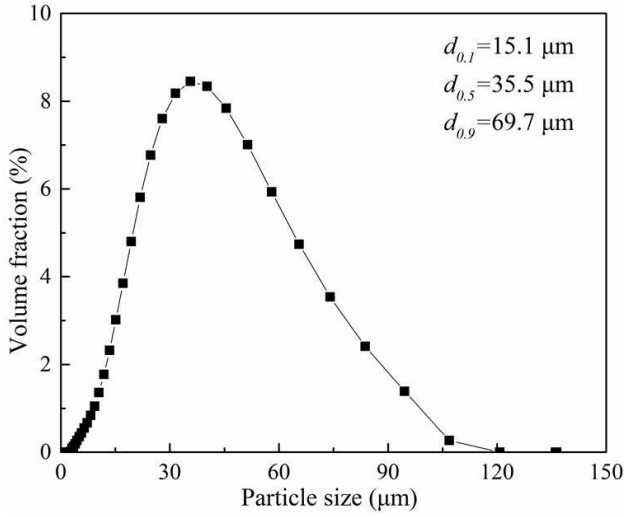

428

429 Fig. 3 The size distribution of the used Muntz powder.

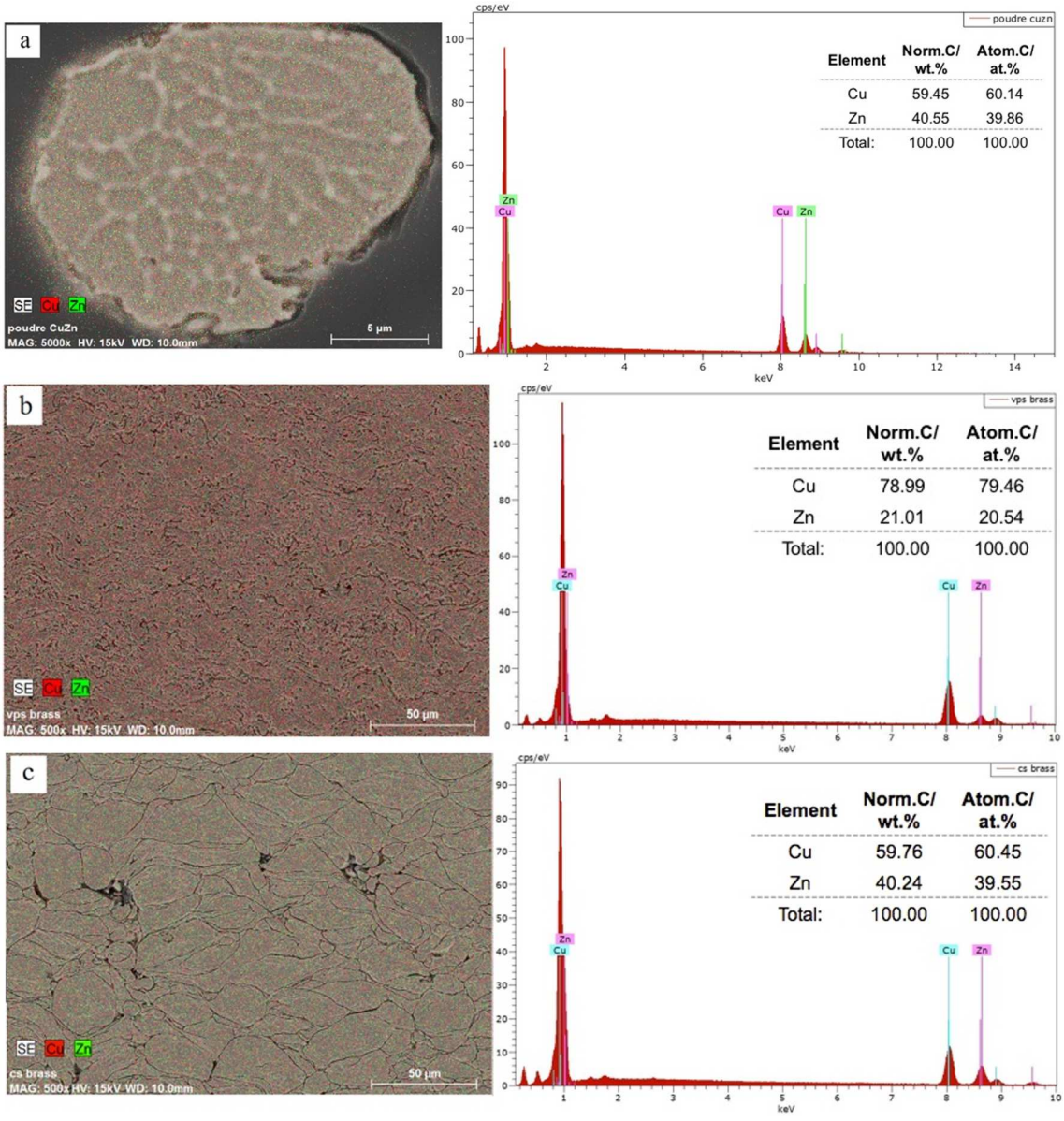

430

431 Fig. 4. EDS maps and element compositions of (a) Muntz powder, (b) VPSed and (c) CGDSed coatings.

432

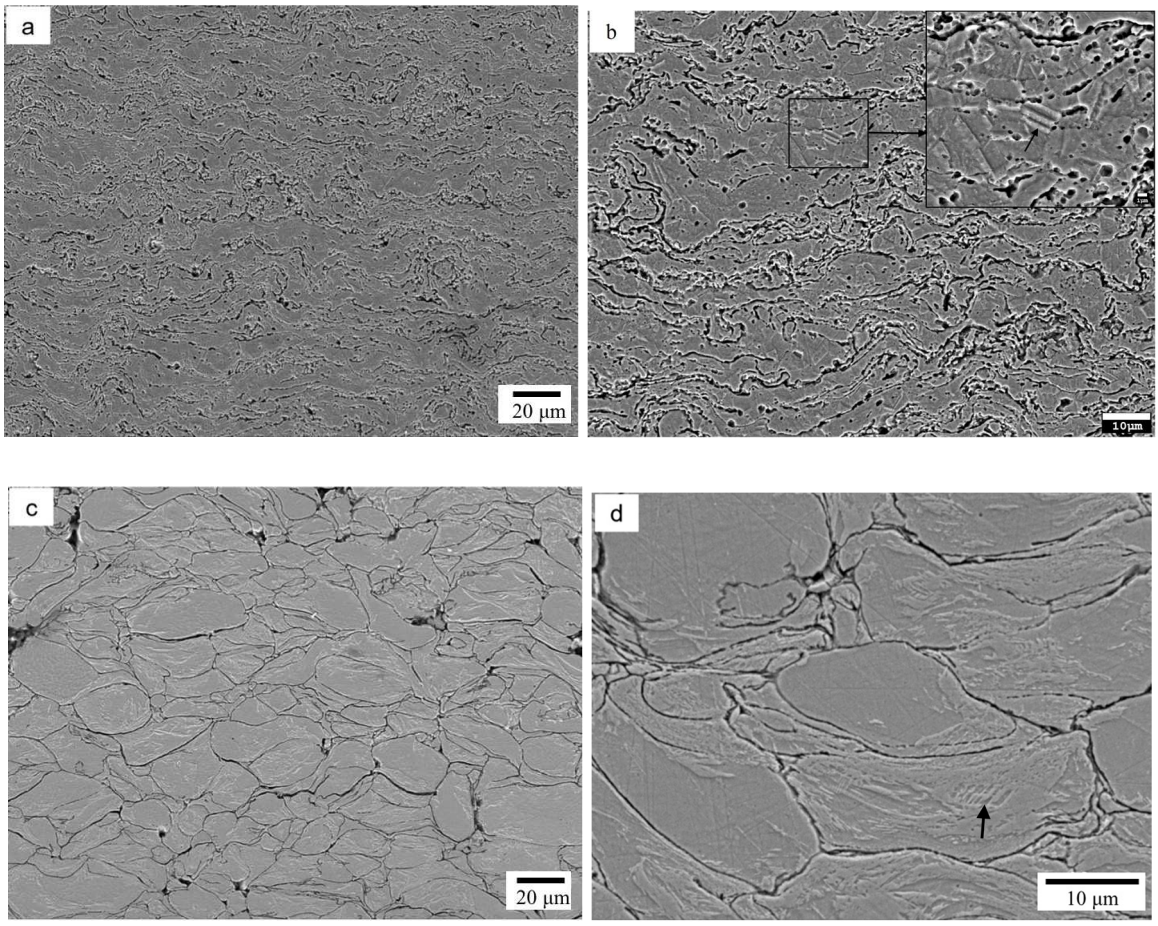

433

434

435 Fig. 5. SEM micrographs of (a and b) VPSed and (c and d) CGDSed Cu60Zn40 coatings.

436

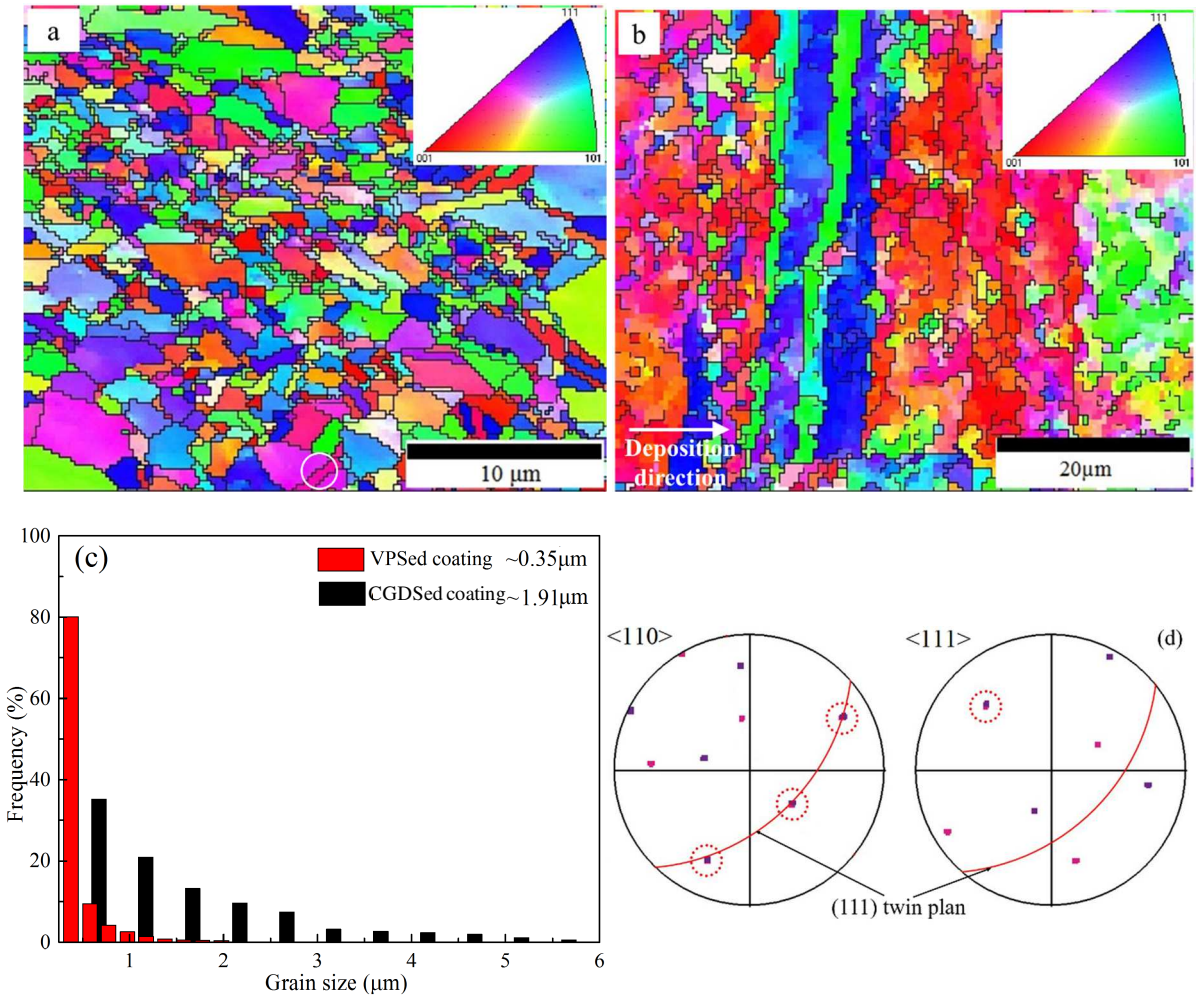

Fig. 6. EDSD maps for (a) VPSed and (b) CGDSed coatings, (c) grain size distribution of these two coatings, and (d) pole figures obtained from the white circle in (a), the common, <110> and <111> directions are marked with small circles. The red circular arcs represent the (111) twin planes.

442

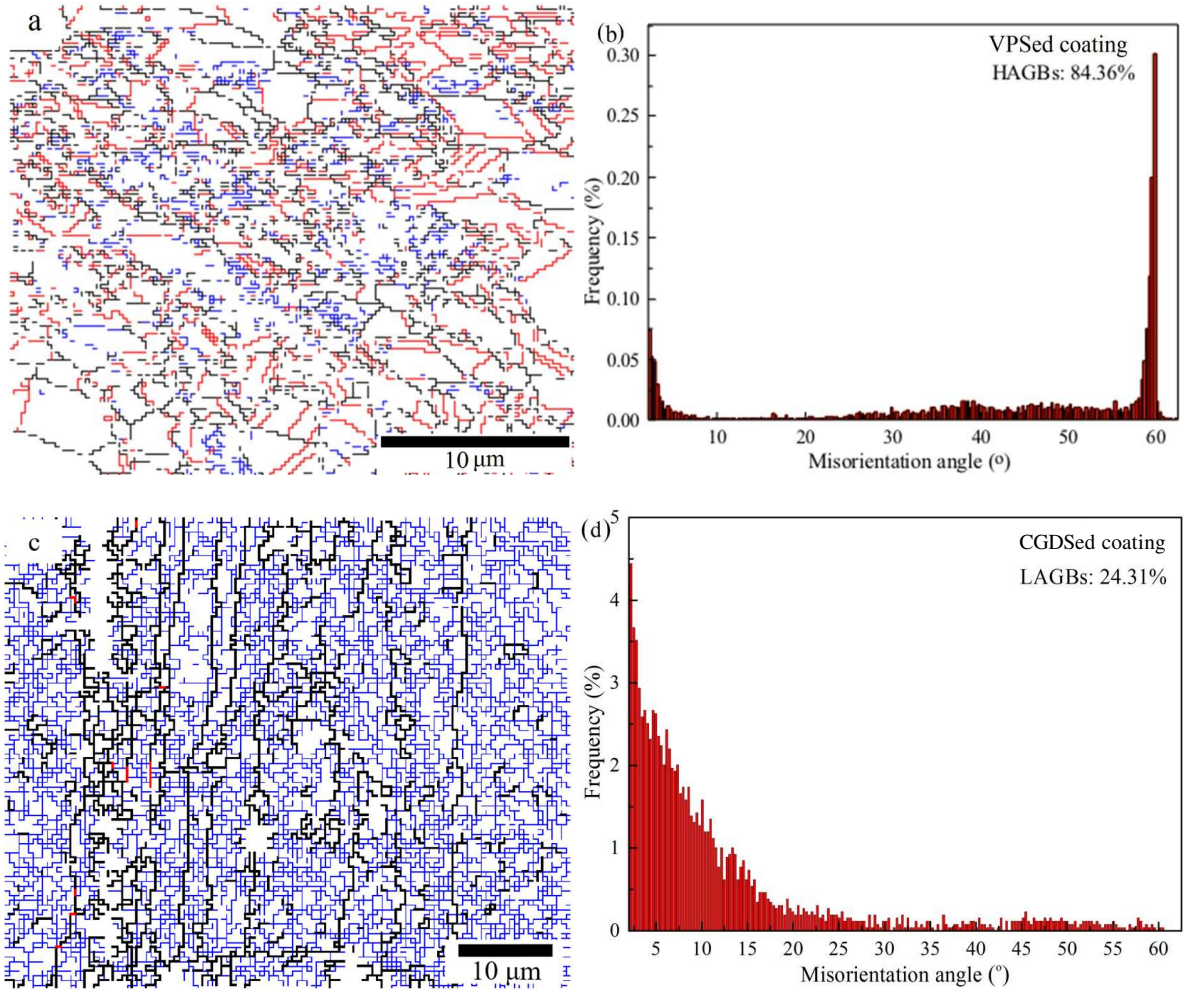

443

444 Fig. 7. Grain boundary maps of (a) VPSed and (c) CSed coatings, the black, blue and red lines in EBSD maps

445 corresponding to the HAGBs ($\theta \geq 15^{o}$), LAGBs ($15^{o} > \theta > 2^{o}$), and (twinned boudaries) TBs, respectively.

446 Misorientation angle distribution of (b) VPSed and (d) CGDSed coatings.

447

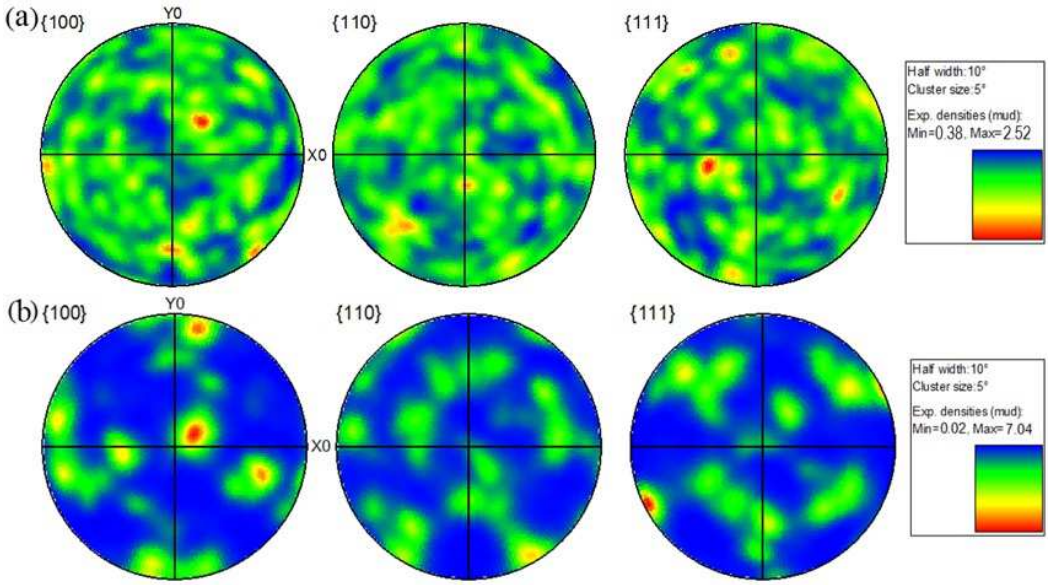

448

449 Fig. 8. Pole figures of (a) VPSed and (b) CGDSed coatings.

450

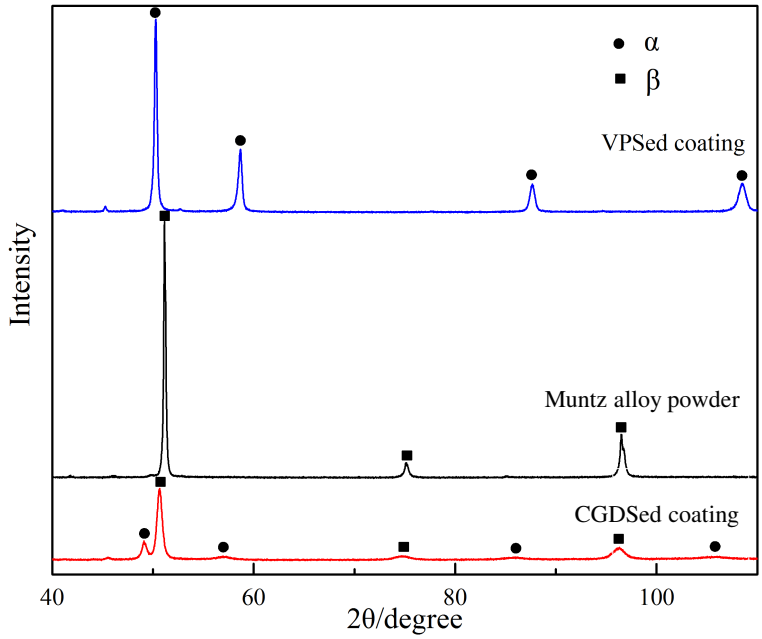

451

452 Fig. 9. XRD patterns of Muntz alloy powder, VPSed and CGDSed coatings.

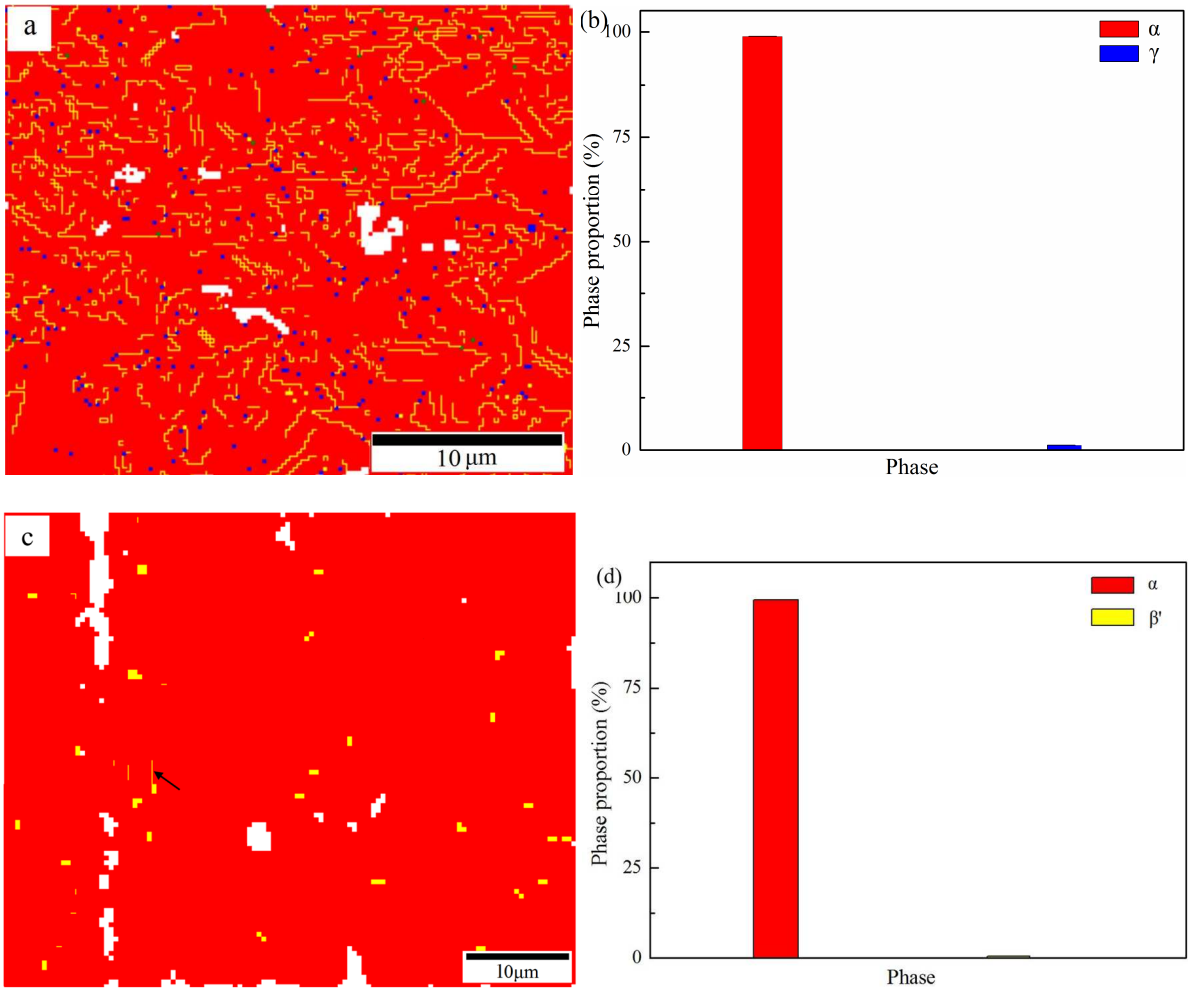

Fig. 10. Phase maps of (a) VPSed and (c) CGDSed coatings [22] , and their phase proportions (b) and (d). The yellow lines in (a) and (c) in EBSD maps corresponding to the TBs, and the red, bule and yellow regions with respective to the α, γ and β' phases.

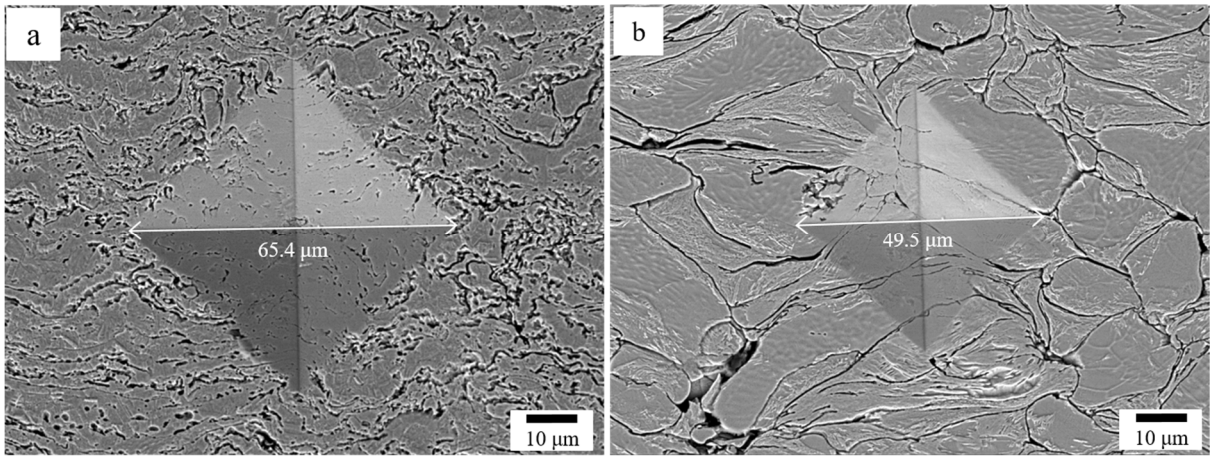

Fig. 11. Cross-sectional SEM micrographs of VPSed and CGDSed coatings after indentation.

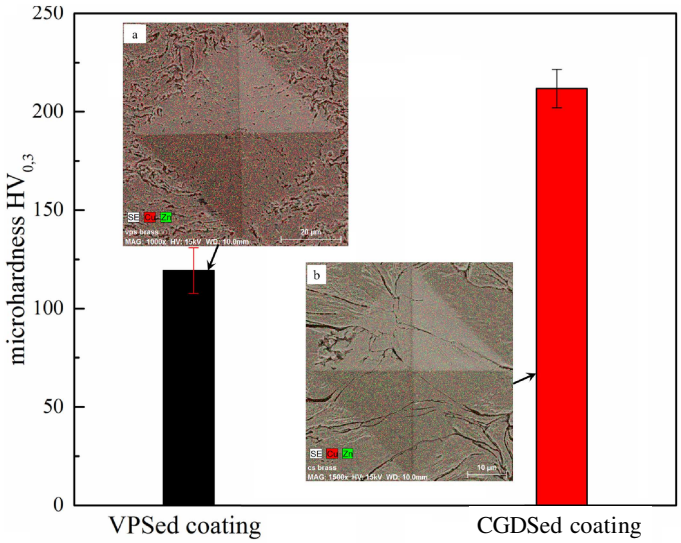

460

461 Fig. 12. Microhardness of VPSed and CGDSed coatings and corresponding indentations analyzed by EDS.

462

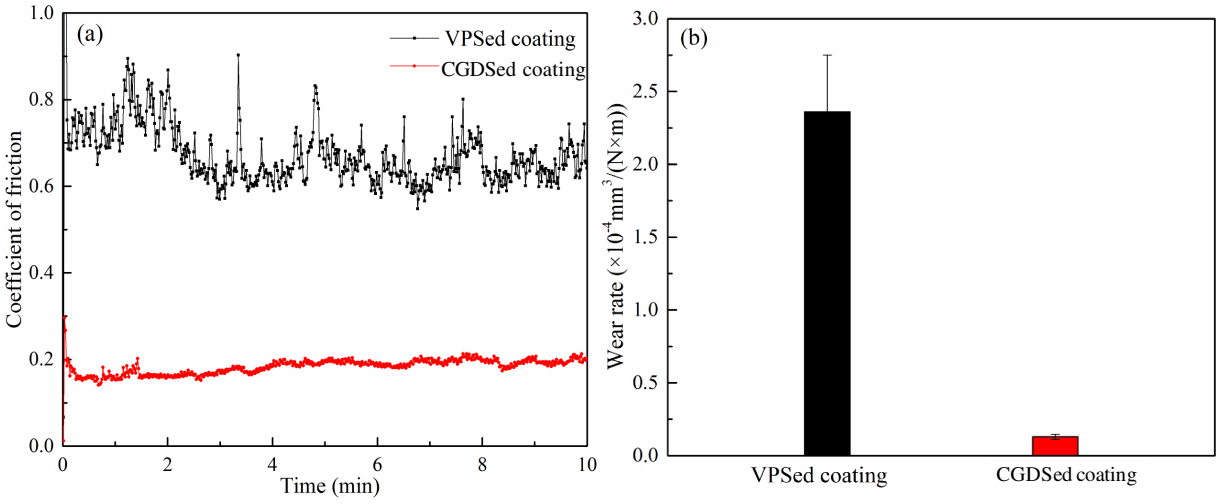

463

464 Fig. 13. Variation of COFs (a) and wear rate (b) of VPSed and CGDSed coatings with sliding time

465 of 10 min at room temperature.

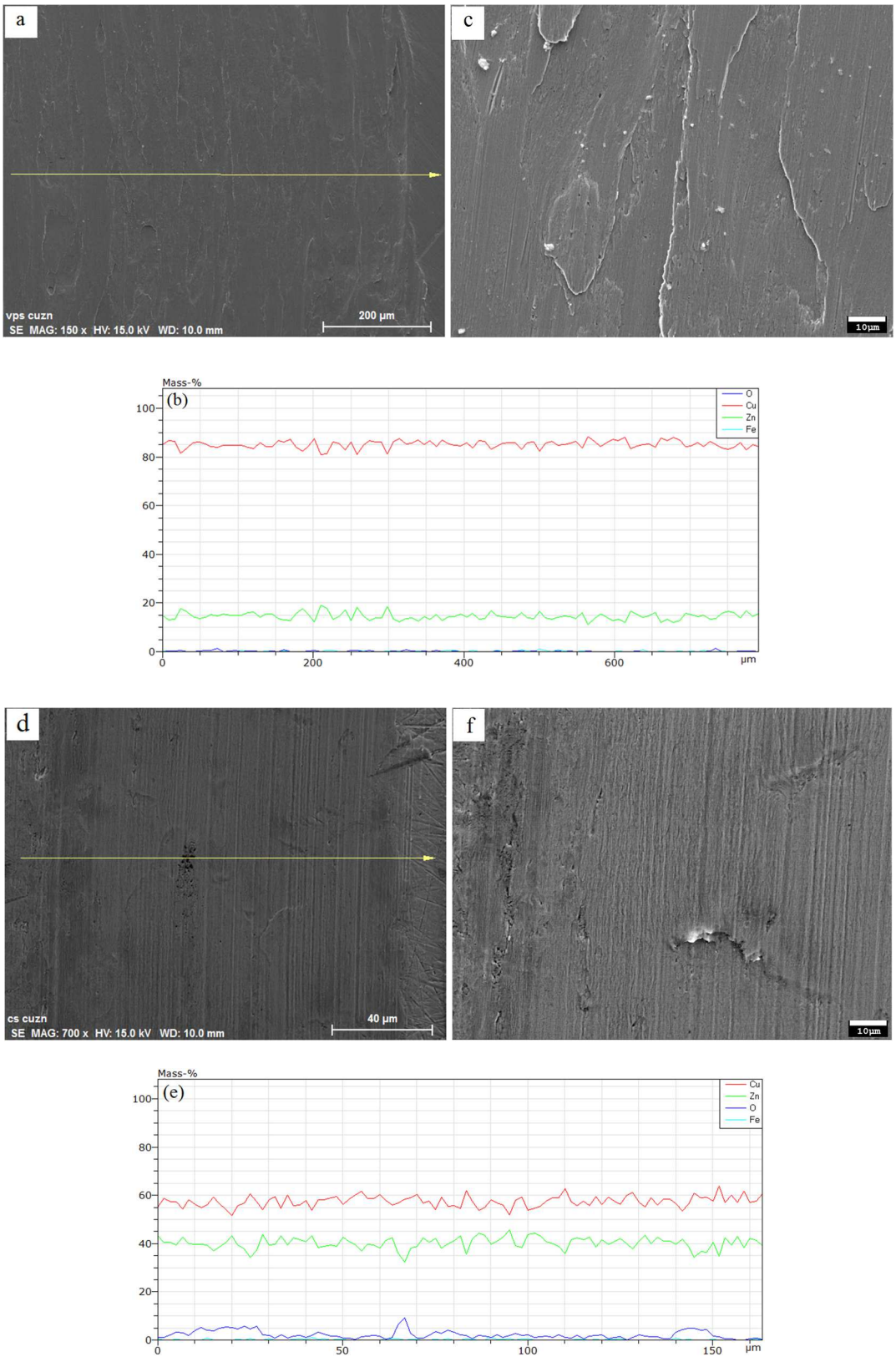

Fig. 14. Worn surfaces morphologies of (a and c) VPSed and (d and f) CGDSed coatings. (b and e) showing the EDS line profiles obtained form (a and d).

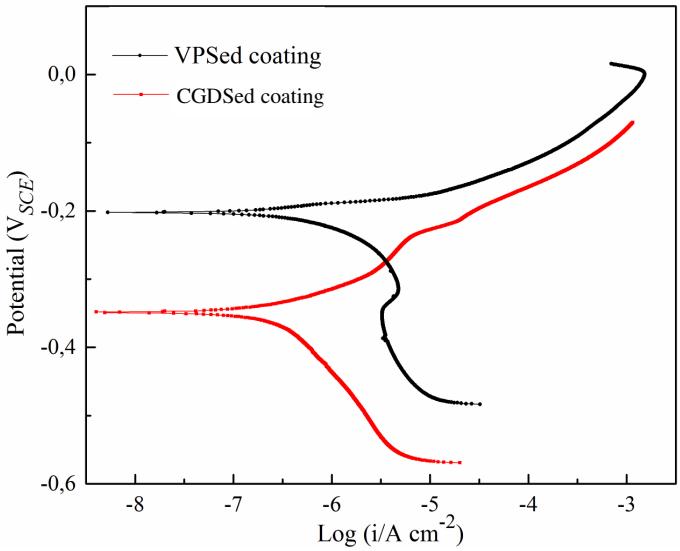

473

474 Fig. 15. Tafel polarization curves of (a) VPSed and (b) CGDSed coatings.

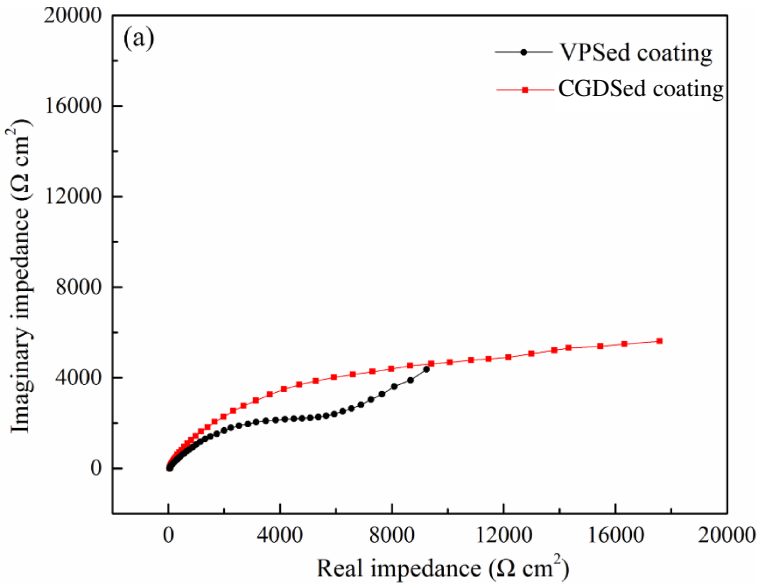

475

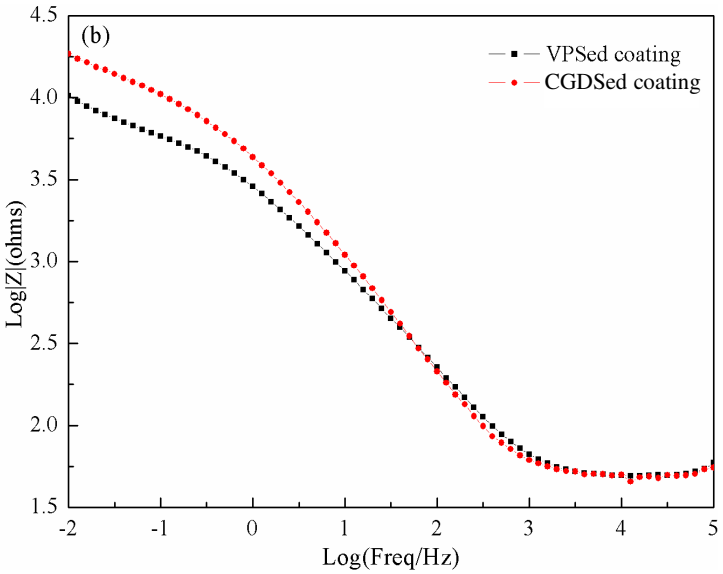

476

477 Fig. 16. Nyquist (a) and Bode (b) plots of the VPSed and CGDSed coatings.